

Moiré Flat Bands of Twisted Few-layer Graphite

Zhen Ma,¹ Shuai Li,¹ Meng-Meng Xiao,¹ Ya-Wen Zheng,¹
Ming Lu,^{3,2} HaiWen Liu,⁵ Jin-Hua Gao,^{1,*} and X. C. Xie^{2,3,4}

¹*School of Physics and Wuhan National High Magnetic Field Center, Huazhong University of Science and Technology, Wuhan 430074, China*

²*International Center for Quantum Materials, School of Physics, Peking University, Beijing 100871, China*

³*Beijing Academy of Quantum Information Sciences, Beijing 100193, China*

⁴*CAS Center for Excellence in Topological Quantum Computation, University of Chinese Academy of Sciences, Beijing 100190, China*

⁵*Center for Advanced Quantum Studies, Department of Physics, Beijing Normal University, Beijing 100875, China*

We report that the twisted few layer graphite (tFL-graphite) is a new family of moiré heterostructures (MHSs), which has richer and highly tunable moiré flat band structures entirely distinct from all the known MHSs. A tFL-graphite is composed of two few-layer graphite (Bernal stacked multilayer graphene), which are stacked on each other with a small twisted angle. The moiré band structure of the tFL-graphite strongly depends on the layer number of its composed two van der Waals layers. Near the magic angle, a tFL-graphite always has two nearly flat bands coexisting with a few pairs of narrowed dispersive (parabolic or linear) bands at the Fermi level, thus, enhances the DOS at E_F . This coexistence property may also enhance the possible superconductivity as been demonstrated in other multiband superconductivity systems. Therefore, we expect strong multiband correlation effects in tFL-graphite. Meanwhile, a proper perpendicular electric field can induce several isolated nearly flat bands with nonzero valley Chern number in some simple tFL-graphites, indicating that tFL-graphite is also a novel topological flat band system.

Introduction.—Moiré heterostructures (MHSs) have drawn great research interest recently [1–8]. The celebrated example is the twisted bilayer graphene (TBG), in which two atomically thin van der Waals (vdW) layers, *i.e.* graphene monolayers here, are stacked with a controlled twist angle θ . A small twist angle results in a long period moiré superlattice. Most importantly, the moiré interlayer hopping (MIH) will give rise to two nearly flat bands, when θ approaches the so-called magic angles [9–14]. Due to the divergent DOS of the moiré flat bands, exotic correlation phenomena, *e.g.* superconductivity and Mott insulator, have been observed in experiments [1–7], and intensively studied with various theoretical methods [15–28].

Further studies indicate that the moiré flat bands exist in a variety of MHSs, such as twisted double bilayer graphene [29–39], twisted trilayer graphene [40–47], twisted rhombohedral (ABC) multilayer graphene [48], trilayer graphene on boron nitride [49–51] and transition metal dichalcogenide heterostructures [52–57]. Note that, in all the above-mentioned MHSs, the low energy moiré band structures are in some sense similar, *i.e.*, two moiré flat bands at the charge neutrality point isolated from other high energy bands. This is because that their vdW layers, like graphene monolayer, bilayer, ABC stacked multilayer, *etc.*, just happen to have two low energy bands near the Fermi level E_F , which are hybridized by the MIH to form the two flat bands. In this work, we report a new family of moiré flat band systems, *twisted few-layer graphite* (tFL-graphite), which have richer and highly controllable moiré flat band structures entirely distinct from all the known MHSs.

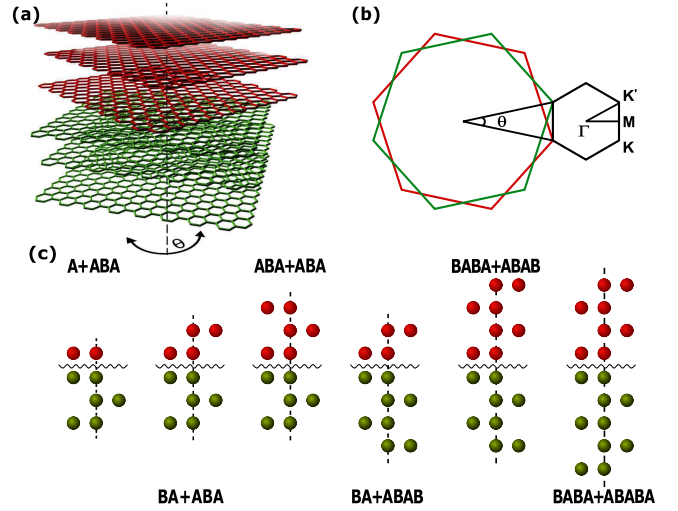


FIG. 1. (a) Schematic of the tFL-graphite, red (green) is the top (bottom) vdW layer. (b) Moiré Brillouin zone (black), red (green) is the first BZ of the top (bottom) vdW layer. (c) Side view of several tFL-graphite configurations.

Typical tFL-graphites are shown in Fig. 1. Here, few layer graphite (FL-graphite) refers to multilayer graphene with Bernal (AB) stacking, in contrast to that with rhombohedral one. Generally, a $M+N$ tFL-graphite is composed of two FL-graphites (red and green in Fig. 1) stacked on top of each other with a twist angle θ , where M (N) is the layer number of the top (bottom) FL-graphite. We assume that $N \geq M$ without loss of generality, and only focus on the cases with $N \geq 3$. So, the simplest tFL-graphite here is the A+ABA (or 1+3) configuration,

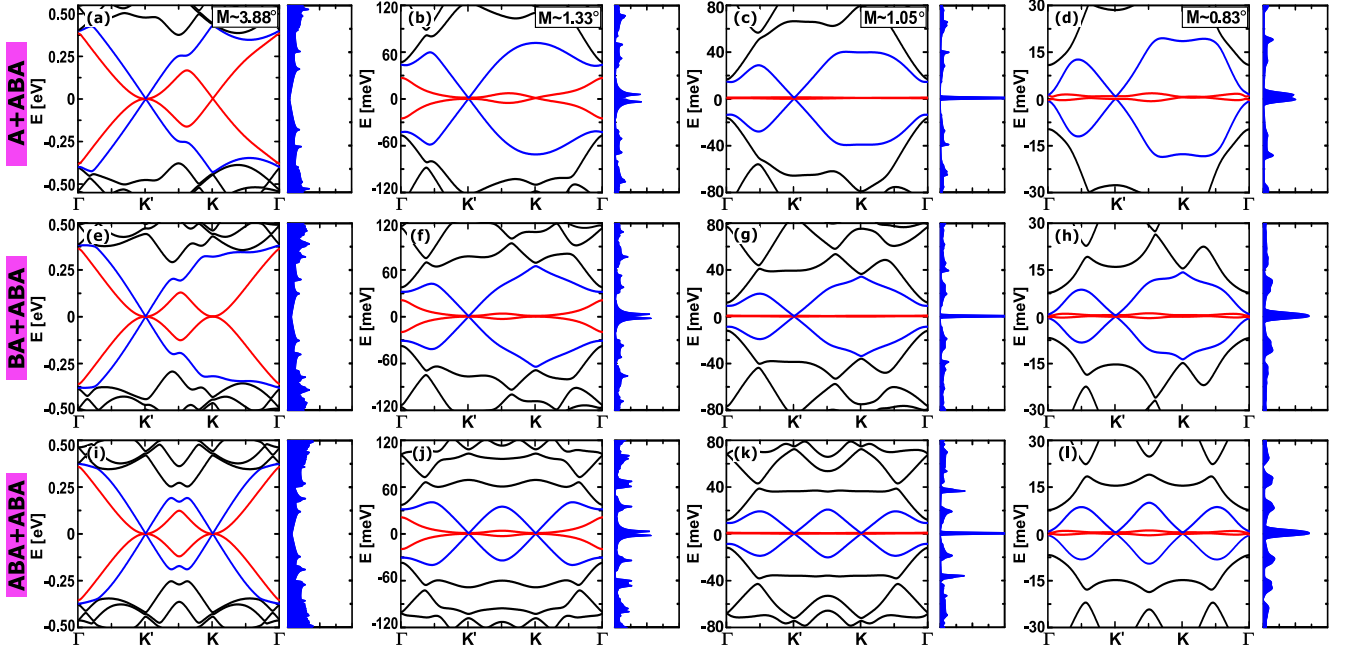


FIG. 2. (a-d), (e-h) and (i-l) are the moiré bands of the A+ABA, BA+ABA and ABA+ABA, respectively. (a, e, i) are calculated at $\theta = 3.88^\circ$; (b, f, j) are calculated at $\theta = 1.33^\circ$; (c, g, k) are calculated at $\theta = 1.05^\circ$; (d, h, l) are calculated at $\theta = 0.83^\circ$. The moiré bands of AB+ABA and BAB+ABA are given in Ref. 58. Parameters: $\omega_1/\omega_2/\gamma_0/\gamma_1/\gamma_3/\gamma_4 = 78/98/2610/360/0/0$ meV, $\xi = -1$ [36, 48].

where A is the top monolayer (red) and ABA is the bottom ABA stacked trilayer (green) [see Fig. 1 (c)].

The distinct moiré band structure of tFL-graphite mainly results from the richer electronic structure of FL-graphite. It is known that a N -layer FL-graphite has $N/2$ electron-like bands and $N/2$ hole-like bands touching at the Dirac points if N is even, while an additional pair of linear bands appears for an odd N [59–61]. Thus, it is natural to expect a rather different moiré band structure in the tFL-graphite. And, as we will see later, twist actually has different influences on the bands of FL-graphite.

We theoretically calculate the electronic structures of tFL-graphites based on a continuum model. Our results show that the electronic structure of a tFL-graphite strongly depends on the layer number of its composed vdW layers, which always has two moiré flat bands coexisting with a few pair of parabolic (or linear) narrow bands near the magic angle. For a $M+N$ tFL-graphite, the main characteristics of its moiré band structures are summarized as follows: (1) The number of the moiré bands at E_F is determined by N , *i.e.* the layer number of the thicker vdW layer, where it has $N(N+1)$ moiré bands if N is even (odd); (2) Near the magic angle (about 1.05°), two of these moiré bands become flat, while others are still parabolic or linear at the Dirac points with narrowed bandwidth; (3) We can get four isolated nearly flat bands with various nonzero valley Chern number by applying a proper electric field in the $N=3$ cases.

Due to the unique electronic structures, the tFL-

graphite has several great advantages as an intriguing MHS. (1) It has a richer and more flexible moiré band structure than the known MHSs, which can be dramatically changed by choosing different layer number. (2) The coexistence of flat bands and other dispersive bands will not only enhance the density of states (DOS) at E_F , but also may meet the demand for the enhancement of superconductivity according to the steep band/flat band scenario [62, 63]. Both these two points imply that stronger multiband correlation effects, *e.g.* superconductivity at higher temperature, may occur in the tFL-graphite. (3) It is a promising platform to study correlation effects in topological bands. (4) The sample preparation of tFL-graphite may not be too challenging [64]. Note that natural graphite is Bernal stacked (more stable than the ABC graphene multilayers), and FL-graphite can be directly obtained by mechanical exfoliation.

Continuum model.—Similar as the TBG, the required θ in the commensurate cases is determined by an integer m , where $\cos\theta = (3m^2 + 3m + \frac{1}{2})/(3m^2 + 3m + 1)$. The corresponding lattice vectors of the moiré supercell are $\mathbf{t}_1 = m\mathbf{a}_1 + (m+1)\mathbf{a}_2$ and $\mathbf{t}_2 = -(m+1)\mathbf{a}_1 + (2m+1)\mathbf{a}_2$, while $\mathbf{a}_1 = a(1/2, \sqrt{3}/2)$ and $\mathbf{a}_2 = a(-1/2, \sqrt{3}/2)$ are the lattice vectors of graphene with lattice constant $a \approx 0.246$ nm. The moiré Brillouin zone (BZ) is given in Fig. 1 (b), which is determined by the BZ of the top vdW layer (red) and that of the bottom layer (green). The reciprocal lattice vectors \mathbf{G}_i can be obtained from $\mathbf{G}_i \cdot \mathbf{t}_j = 2\pi\delta_{ij}$, and K (K') is the Dirac point

corresponding to the top (bottom) layer [see Fig. 1 (b)].

The effective continuum model is used to describe the tFL-graphite [10–12]. For a M+N tFL-graphite, the Hamiltonian is

$$H_{M+N}(\theta) = \begin{pmatrix} H_N(k_1) & T(r) \\ T^\dagger(r) & H_M(k_2) \end{pmatrix} + U \quad (1)$$

where $k_1 = R(-\theta/2)(k - K)$, $k_2 = R(\theta/2)(k - K')$ and $R(\theta)$ is the rotation matrix. H_M (H_N) is the Hamiltonian of M-layer (N-layer) FL-graphite [59–61, 65]. For example, $H_{N=3}$ is the Hamiltonian of the ABA trilayer

$$H_{N=3}(k) = \begin{pmatrix} h_0(k) & g(k)^\dagger & 0 \\ g(k) & h_0(k) & g(k) \\ 0 & g(k)^\dagger & h_0(k) \end{pmatrix}, \quad (2)$$

where $h_0(\mathbf{k}) = -\hbar v_F \mathbf{k} \cdot \boldsymbol{\sigma}$ is the low-energy effective Hamiltonian for graphene monolayer and $g(k)$ is the interlayer hopping

$$g(k) = \begin{pmatrix} \hbar v_4 k_+ & \gamma_1 \\ \hbar v_3 k_- & \hbar v_4 k_+ \end{pmatrix}. \quad (3)$$

Here, $k_\pm = \xi k_x \pm i k_y$, with $\xi = \pm 1$ for the two different valley in multilayer graphene. γ_1 is the vertical hopping and $v_i = \frac{\sqrt{3}\gamma_i a}{2\hbar}$ ($i=3,4$). γ_3 and γ_4 are the remote interlayer hoppings, which stand for the trigonal warping and electron-hole asymmetry, respectively. The moiré interlayer coupling is $T(r) = \sum_{n=0,1,2} T_n \cdot e^{-iQ_n \cdot r}$, where

$$T_n = I_{MN} \otimes \begin{pmatrix} \omega_1 & \omega_2 e^{in\phi} \\ \omega_2 e^{-in\phi} & \omega_1 \end{pmatrix}. \quad (4)$$

Here, I_{MN} is a $N \times M$ matrix with only one nonzero matrix element $I_{MN}(1, N) = 1$, $\phi = 2\pi/3$, $Q_n = R(n\phi) \cdot (K - K')$. At last, U in Eq. (1) is a diagonal matrix denoting the perpendicular electric field induced potential in layers, where we set the potential difference between adjacent two layers is V [58].

Moiré bands of the simplest tFL-graphite.—Most of the moiré band characteristics of tFL-graphite can be seen from the simplest tFL-graphites, *i.e.*, N=3 and M=(1,2,3). The calculated moiré bands are given in Fig. 2, each row of which corresponds to one structure of tFL-graphite. Here, we use a minimal model, only including the dominating interlayer hopping γ_1 in Eq. (3), to illustrate the ideal flat bands at the magic angle. We also use a full parameter model to account for the realistic situations, where the influence of γ_3 and γ_4 are considered [58]. The first to fourth columns in Fig. 2 are the moiré bands with $\theta = 3.88^\circ$, $\theta = 1.33^\circ$, $\theta = 1.05^\circ$ and $\theta = 0.83^\circ$, respectively. Corresponding DOS is also plotted.

First of all, tFL-graphite has more moiré bands than all the known MHSs at E_F . For example, all the cases (N=3) in Fig. 2 have four moiré bands at E_F , instead of two like in TBG. It is because that the low energy moiré

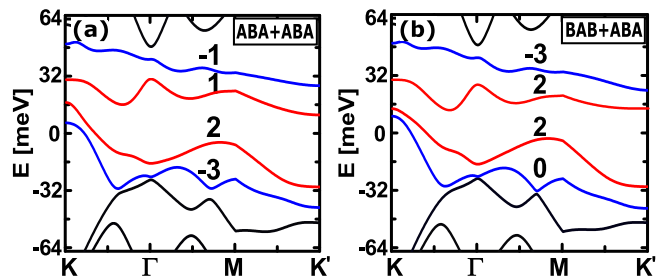


FIG. 3. (a), (b) are the moiré bands under a perpendicular electric field for the ABA+ABA and BAB+ABA, respectively. $V = 20$ meV, $\theta = 1.33^\circ$ and full parameter model is used. The black number are the valley Chern numbers for four moiré bands (red and blue solid lines).

bands of a tFL-graphite are constructed by hybridizing the bands of top and bottom vdW layers near the Dirac points via the MIH. In TBG, each vdW layer has two linear bands near the Dirac point. But in the A+ABA tFL-graphite, the top vdW layer (monolayer) has two linear bands, while the bottom vdW layer (ABA-trilayer) has four bands, *i.e.* a parabolic electron band, a parabolic hole band and a pair of linear bands. As shown in Fig. 2 (a-d), the MIH hybridizes the two parabolic bands of the bottom ABA-trilayer with the two linear bands of the top monolayer (red lines), while the remaining two linear bands of the ABA-trilayer are modified into two other moiré bands at E_F (blue lines). Thus, there are four moiré bands near E_F in the A+ABA tFL-graphite. The moiré bands of BA+ABA [Fig. 2 (e-h)] and ABA+ABA [Fig. 2 (i-l)] tFL-graphites can be understood in a similar way. Generally, for a M+N tFL-graphite, the number of moiré bands at E_F is equal to that of the thicker vdW layer, *i.e.* it has N moiré bands ($N+1$) if N is even (odd) when $N \geq M$. Half of the moiré bands are electron-like and the others are hole-like.

The magic angle of the tFL-graphite is about 1.05° , the same as that of TBG. However, only two of these moiré bands in tFL-graphite can be transformed into flat bands at the magic angle, while others are still dispersive but their bandwidth are greatly narrowed. This is shown clearly in Fig. 2 (c), (g), (k), which are calculated with $\theta = 1.05^\circ$ based on the minimal model. Increasing θ , the bandwidth of the moiré bands becomes larger, and the flat bands become dispersive [see Fig. 2 (b), (f), (j) with $\theta = 1.33^\circ$]. With a twist angle smaller than the magic angle [*e.g.* $\theta = 0.83^\circ$ in Fig. 2 (d), (h), (l)], the flat band [red lines] will become slightly dispersive while the bandwidth of the other two moiré bands [blue lines] are reduced further [smaller than 10 meV in Fig. 2 (l)]. It suggests that the correlation in such narrow dispersive bands may be also very strong with small θ . At large twist angle [*e.g.* Fig. 2 (a), (e), (i) with $\theta = 3.88^\circ$], the shape of the bands near K (K') points recovers to that of the isolated top (bottom) vdW layer. Note that

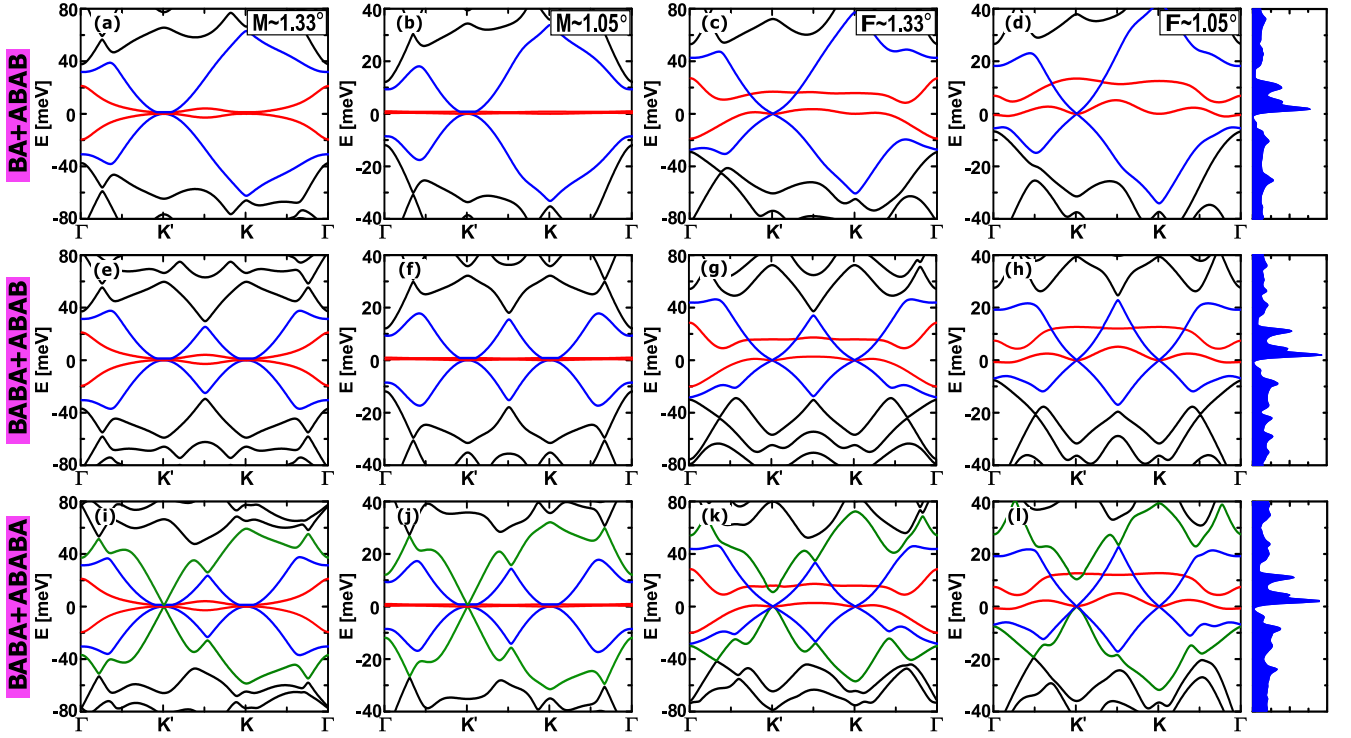


FIG. 4. (a-d), (e-h) and (i-l) are the moiré bands of the BA+ABAB, BABA+ABAB and BABA+ABABA, respectively. (a, e, i) are calculated with the minimal model at $\theta = 1.33^\circ$; (b, f, j) are calculated with minimal model at $\theta = 1.05^\circ$; (c, g, k) are calculated with full parameter model at $\theta = 1.33^\circ$; (d, h, l) are calculated with full parameter model at $\theta = 1.05^\circ$, and the corresponding DOS is also plotted. Parameters: $\omega_1/\omega_2/\gamma_0/\gamma_1/\gamma_3/\gamma_4 = 78/98/2610/360/283/138 \text{ meV}$, $\xi = -1$.

the A+ABA [Fig. 2 (c)] and BA+ABA [Fig. 2 (g)] both host flat bands coexisting with a single Dirac cone (K'), while ABA+ABA [Fig. 2 (k)] have two Dirac cones. This coexistence feature is very interesting because that the simultaneous occurrence of flat and steep bands is a favorable condition to enhance superconductivity, according to the “steep band/flat band” scenario of superconductivity [62, 63]. Note that coexistence of flat band with linear bands at E_F was also noticed in some multi-twist MHSs very recently[43, 44, 66], while only one twist is required here.

The low energy moiré bands of tFL-graphite also exhibit exotic topological properties, the valley Chern number of which can be nonzero. In Fig. 3, we consider two example, *i.e.* ABA+ABA and BAB+ABA. We first see that the four moiré bands at E_F can be isolated by a proper perpendicular electric field, while their bandwidth are still small. For these isolated moiré bands, we calculate their valley Chern numbers with the standard formula [58], which are indicated by black numbers in Fig. 3. The first interesting issue is that tFL-graphite here have four moiré bands with nonzero valley Chern number, while other known MHSs only have two [33, 34, 40, 48, 49]. Furthermore, despite that ABA+ABA and BAB+ABA differ only in the relative orientation and have very similar band structure [58],

their moiré bands have different valley Chern number. The cases of AB+ABA and BA+ABA are similar, and the valley Chern number is controllable by the twist angle and perpendicular electric field [58].

Moiré bands of thicker tFL-graphite.—Now we study the moiré bands of thicker tFG-graphites. Several typical examples are given in Fig. 4. These thicker tFL-graphites have various moiré bands near the E_F , depending on their own layer numbers. For example, with $N=4$ (BA+ABAB, BABA+ABAB), there exists a pair of flat bands (red lines) coexisting with a parabolic electron and a parabolic hole bands (blue lines), as shown in Fig. 4 (a-b) and (e-f). Compared with the $N=3$ cases in Fig. 2, the parabolic bands here can obviously enhance the DOS at E_F , which indicates that correlation effects in thicker tFL-graphite may be stronger. Increasing the layer number further, it is able to induce more moiré bands near the E_F . A $N=5$ example is given in Fig.4 (i-j), which has six moiré bands including a pair of flat bands, two parabolic bands and two linear bands (green lines).

Note that the influence of the remote hopping γ_3 and γ_4 is critical, and different on various moiré bands, as illustrated by the full parameter model calculations in Fig. 4 (c-d), (g-h) and (k-l). The remote hopping always separates the the flat bands in energy (red lines) and make them dispersive. But it does not significantly

modify the parabolic bands near the Dirac points (blue lines). Meanwhile, a gap at the Dirac points is induced to the linear bands in $N=5$ case [see in Fig. 4 (k-l), green lines].

Summary.—Our numerical calculations reveal and give some intuitive understanding about the unique, richer and highly controllable the moiré flat band structure in tFL-graphite, which may be directly verified by the nano-ARPES technique [67–71]. However, the research on the moiré bands in tFL-graphite is still at early stage, though the FL-graphite has been studied for rather a long time [64, 72–75]. Many basic problems are still unknown. For example, why does twist have different influences on the bands of FL-graphite? Whether can the multiband feature here significantly enhance the superconductivity? We hope our study will stimulate further interest on this promising system with moiré multiband correlations.

We thank Jinhua Sun for helpful discussion. This work is supported by the National Natural Science Foundation of China (Grants No. 11534001, 11874160, 11274129, 11874026, 61405067), and the Fundamental Research Funds for the Central Universities (HUST: 2017KFYXJJ027), and NBRPC (Grants No. 2015CB921102).

* jinhua@hust.edu.cn

- [1] Y. Cao, V. Fatemi, A. Demir, S. Fang, S. L. Tomarken, J. Y. Luo, J. D. Sanchez-Yamagishi, K. Watanabe, T. Taniguchi, E. Kaxiras, R. C. Ashoori, and P. Jarillo-Herrero, *Nature* **556**, 80 (2018).
- [2] Y. Cao, V. Fatemi, S. Fang, K. Watanabe, T. Taniguchi, E. Kaxiras, and P. Jarillo-Herrero, *Nature* **556**, 43 (2018).
- [3] M. Yankowitz, S. Chen, H. Polshyn, Y. Zhang, K. Watanabe, T. Taniguchi, D. Graf, A. F. Young, and C. R. Dean, *Science* **363**, 1059 (2019).
- [4] X. Lu, P. Stepanov, W. Yang, M. Xie, M. Aamir, I. Das, C. Urgell, K. Watanabe, T. Taniguchi, G. Zhang, A. Bachtold, A. MacDonald, and D. Efetov, *Nature* **574**, 653 (2019).
- [5] A. Sharpe, E. Fox, A. Barnard, J. Finney, K. Watanabe, T. Taniguchi, M. Kastner, and D. Goldhaber-Gordon, *Science* **365**, 605 (2019).
- [6] E. Codecido, Q. Wang, R. Koester, S. Che, H. Tian, R. Lv, S. Tran, K. Watanabe, T. Taniguchi, F. Zhang, M. Bockrath, and C. Lau, *Sci. Adv.* **5** (2019).
- [7] Y. Jiang, X. Lai, K. Watanabe, T. Taniguchi, K. Haule, J. Mao, and E. Andrei, *Nature* **573**, 91 (2019).
- [8] Q. Tong, H. Yu, Q. Zhu, Y. Wang, X. Xu, and W. Yao, *Nat. Phys.* **13**, 356 (2017).
- [9] J. M. B. Lopes dos Santos, N. M. R. Peres, and A. H. Castro Neto, *Phys. Rev. Lett.* **99**, 256802 (2007).
- [10] R. Bistritzer and A. H. MacDonald, *Proc. Natl. Acad. Sci.* **108**, 12233 (2011).
- [11] J. M. B. Lopes dos Santos, N. M. R. Peres, and A. H. Castro Neto, *Phys. Rev. B* **86**, 155449 (2012).
- [12] P. Moon and M. Koshino, *Phys. Rev. B* **87**, 205404 (2013).
- [13] M. Koshino, N. F. Q. Yuan, T. Koretsune, M. Ochi, K. Kuroki, and L. Fu, *Phys. Rev. X* **8**, 031087 (2018).
- [14] J. Kang and O. Vafek, *Phys. Rev. X* **8**, 031088 (2018).
- [15] L. A. Gonzalez-Arraga, J. L. Lado, F. Guinea, and P. San-Jose, *Phys. Rev. Lett.* **119**, 107201 (2017).
- [16] C. Xu and L. Balents, *Phys. Rev. Lett.* **121**, 087001 (2018).
- [17] H. C. Po, L. Zou, A. Vishwanath, and T. Senthil, *Phys. Rev. X* **8**, 031089 (2018).
- [18] H. Isobe, N. F. Q. Yuan, and L. Fu, *Phys. Rev. X* **8**, 041041 (2018).
- [19] B. Padhi, C. Setty, and P. Phillips, *Nano Lett.* **18**, 6175 (2018).
- [20] F. Guinea and N. Walet, *Proc. Natl. Acad. Sci.* **115**, 13174 (2018).
- [21] C.-C. Liu, L.-D. Zhang, W.-Q. Chen, and F. Yang, *Phys. Rev. Lett.* **121**, 217001 (2018).
- [22] H. Guo, X. Zhu, S. Feng, and R. T. Scalettar, *Phys. Rev. B* **97**, 235453 (2018).
- [23] Y.-P. Lin and R. M. Nandkishore, *Phys. Rev. B* **98**, 214521 (2018).
- [24] F. Wu, A. H. MacDonald, and I. Martin, *Phys. Rev. Lett.* **121**, 257001 (2018).
- [25] B. Lian, Z. Wang, and B. A. Bernevig, *Phys. Rev. Lett.* **122**, 257002 (2019).
- [26] T. J. Peltonen, R. Ojajärvi, and T. T. Heikkilä, *Phys. Rev. B* **98**, 220504 (2018).
- [27] D. M. Kennes, J. Lischner, and C. Karrasch, *Phys. Rev. B* **98**, 241407 (2018).
- [28] Y.-Z. You and A. Vishwanath, *Npj Quantum Mater.* **4**, 16 (2019).
- [29] X. Liu, Z. Hao, E. Khalaf, J. Lee, Y. Ronen, H. Yoo, D. Najafabadi, K. Watanabe, T. Taniguchi, A. Vishwanath, and P. Kim, *Nature* **583**, 221 (2020).
- [30] C. Shen, Y. Chu, Q. Wu, N. Li, S. Wang, Y. Zhao, J. Tang, J. Liu, J. Tian, K. Watanabe, T. Taniguchi, R. Yang, Z. Y. Meng, D. Shi, O. V. Yazyev, and G. Zhang, *Nat. Phys.* **16**, 520 (2020).
- [31] Y. Cao, D. Rodan-Legrain, O. Rubies-Bigorda, J. M. Park, K. Watanabe, T. Taniguchi, and P. Jarillo-Herrero, *Nature* **583**, 215 (2020).
- [32] G. W. Burg, J. Zhu, T. Taniguchi, K. Watanabe, A. H. MacDonald, and E. Tutuc, *Phys. Rev. Lett.* **123**, 197702 (2019).
- [33] Y.-H. Zhang, D. Mao, Y. Cao, P. Jarillo-Herrero, and T. Senthil, *Phys. Rev. B* **99**, 075127 (2019).
- [34] M. Koshino, *Phys. Rev. B* **99**, 235406 (2019).
- [35] N. R. Chebrolu, B. L. Chittari, and J. Jung, *Phys. Rev. B* **99**, 235417 (2019).
- [36] J. Y. Lee, E. Khalaf, S. Liu, X. Liu, Z. Hao, P. Kim, and A. Vishwanath, *Nat. Commun.* **10** (2019).
- [37] F. Haddadi, Q. Wu, A. J. Kruchkov, and O. V. Yazyev, *Nano Lett.* **20**, 2410 (2020).
- [38] F. Wu and S. Das Sarma, *Phys. Rev. B* **101**, 155149 (2020).
- [39] F. J. Culchac, R. B. Capaz, L. Chico, and E. Suarez Morell, [arXiv:1911.01347](https://arxiv.org/abs/1911.01347).
- [40] Z. Ma, S. Li, Y.-W. Zheng, M.-M. Xiao, H. Jiang, J.-H. Gao, and X. C. Xie, [arXiv:1905.00622](https://arxiv.org/abs/1905.00622).
- [41] W.-J. Zuo, J.-B. Qiao, D.-L. Ma, L.-J. Yin, G. Sun, J.-Y. Zhang, L.-Y. Guan, and L. He, *Phys. Rev. B* **97**, 035440 (2018).
- [42] E. Suárez Morell, M. Pacheco, L. Chico, and L. Brey,

- Phys. Rev. B* **87**, 125414 (2013).
- [43] X. Li, F. Wu, and A. H. MacDonald, [arXiv:1907.12338](#).
- [44] S. Carr, C. Li, Z. Zhu, E. Kaxiras, S. Sachdev, and A. Kruchkov, *Nano Lett.* **20**, 3030 (2020).
- [45] Y. Shi, S. Xu, M. M. Al Ezzi, N. Balakrishnan, A. Garcia-Ruiz, B. Tsim, C. Mullan, J. Barrier, N. Xin, B. A. Piot, T. Taniguchi, K. Watanabe, A. Carvalho, A. Mishchenko, A. K. Geim, V. I. Fal'ko, S. Adam, A. Helio Castro Neto, and K. S. Novoselov, [arXiv:2004.12414](#).
- [46] S. Chen, M. He, Y.-H. Zhang, V. Hsieh, Z. Fei, K. Watanabe, T. Taniguchi, D. H. Cobden, X. Xu, C. R. Dean, and M. Yankowitz, [arXiv:2004.11340](#).
- [47] H. Polshyn, J. Zhu, M. A. Kumar, Y. Zhang, F. Yang, C. L. Tschirhart, M. Serlin, K. Watanabe, T. Taniguchi, A. H. MacDonald, and A. F. Young, [arXiv:2004.11353](#).
- [48] J. Liu, Z. Ma, J. Gao, and X. Dai, *Phys. Rev. X* **9**, 031021 (2019).
- [49] B. L. Chittari, G. Chen, Y. Zhang, F. Wang, and J. Jung, *Phys. Rev. Lett.* **122**, 016401 (2019).
- [50] G. Chen, L. Jiang, S. Wu, B. Lyu, H. Li, B. L. Chittari, K. Watanabe, T. Taniguchi, Z. Shi, J. Jung, Y. Zhang, and F. Wang, *Nat. Phys* **15**, 237 (2019).
- [51] G. Chen, A. Sharpe, P. Gallagher, I. Rosen, E. Fox, L. Jiang, B. Lyu, H. Li, K. Watanabe, T. Taniguchi, J. Jung, Z. Shi, D. Goldhaber-Gordon, Y. Zhang, and F. Wang, *Nature* **572**, 215 (2019).
- [52] F. Wu, T. Lovorn, E. Tutuc, and A. H. MacDonald, *Phys. Rev. Lett.* **121**, 026402 (2018).
- [53] M. H. Naik and M. Jain, *Phys. Rev. Lett.* **121**, 266401 (2018).
- [54] Y. Pan, S. Flsch, Y. Nie, D. Waters, Y.-C. Lin, B. Jariwala, K. Zhang, K. Cho, J. Robinson, and R. Feenstra, *Nano Lett.* **18**, 1849 (2018).
- [55] F. Wu, T. Lovorn, E. Tutuc, I. Martin, and A. H. MacDonald, *Phys. Rev. Lett.* **122**, 086402 (2019).
- [56] F. Conte, D. Ninno, and G. Cantele, *Phys. Rev. B* **99**, 155429 (2019).
- [57] S. Javvaji, J.-H. Sun, and J. Jung, *Phys. Rev. B* **101**, 125411 (2020).
- [58] See the Supplemental Material for more details.
- [59] F. Guinea, A. H. Castro Neto, and N. M. R. Peres, *Phys. Rev. B* **73**, 245426 (2006).
- [60] M. Koshino and T. Ando, *Phys. Rev. B* **76**, 085425 (2007).
- [61] H. Min and A. H. MacDonald, *Phys. Rev. B* **77**, 155416 (2008).
- [62] A. Simon, *Angew. Chem.* **36**, 1788 (1997).
- [63] A. Bussmann-Holder, H. Keller, A. Simon, and A. Bianconi, *Condens. Matter* **4**, 91 (2019).
- [64] J.-B. Wu, X. Zhang, M. Ijäs, W.-P. Han, X.-F. Qiao, X.-L. Li, D.-S. Jiang, A. C. Ferrari, and P.-H. Tan, *Nat. Commun.* **5**, 5309 (2014).
- [65] F. Zhang, B. Sahu, H. Min, and A. H. MacDonald, *Phys. Rev. B* **82**, 035409 (2010).
- [66] E. Khalaf, A. J. Kruchkov, G. Tarnopolsky, and A. Vishwanath, *Phys. Rev. B* **100**, 085109 (2019).
- [67] H. Peng, N. Schrter, J. Yin, H. Wang, T.-F. Chung, Y. Haifeng, S. A. Ekahana, Z. Liu, J. Jiang, L. Yang, T. Zhang, C. Chen, H. Ni, A. Barinov, Y. Chen, Z. Liu, H. Peng, and Y. Chen, *Adv Mater.* **29**, 1606741 (2017).
- [68] M. I. B. Utama, R. J. Koch, K. Lee, N. Leconte, H. Li, S. Zhao, L. Jiang, J. Zhu, K. Watanabe, T. Taniguchi, *et al.*, *Nat. Phys.* (2020).
- [69] J. J. P. Thompson, D. Pei, H. Peng, H. Wang, N. Channa, H. L. Peng, A. Barinov, N. B. M. Schröter, Y. Chen, and M. Mucha-Kruczyński, *Nat. Commun.* **11**, 3582 (2020).
- [70] S. Lisi, X. Lu, T. Benschop, T. A. de Jong, P. Stepanov, J. R. Duran, F. Margot, I. Cucchi, E. Cappelli, A. Hunter, A. Tamai, V. Kandyba, A. Giampietri, A. Barinov, J. Jobst, V. Stalman, M. Leeuwenhoek, K. Watanabe, T. Taniguchi, L. Rademaker, S. J. van der Molen, M. Allan, D. K. Efetov, and F. Baumberger, [arXiv:2002.02289](#).
- [71] A. J. H. Jones, R. Muzzio, P. Majchrzak, S. Pakdel, D. Curcio, K. Volckaert, D. Biswas, J. Gobbo, S. Singh, J. T. Robinson, K. Watanabe, T. Taniguchi, T. K. Kim, C. Cacho, N. Lanata, J. A. Miwa, P. Hofmann, J. Katoch, and S. Ulstrup, [arXiv:2006.00791](#).
- [72] A. Vela, M. V. O. Moutinho, F. J. Culchac, P. Venezuela, and R. B. Capaz, *Phys. Rev. B* **98**, 155135 (2018).
- [73] T. Cea, N. Walet, and F. Guinea, *Nano Lett.* **19**, 8683 (2019).
- [74] A. Grushina, D.-K. Ki, M. Koshino, A. Nicolet, C. Faugeras, E. McCann, M. Potemski, and A. Morpurgo, *Nat. Commun.* **6**, 6419 (2015).
- [75] Y. Nam, D.-K. Ki, D. Soler-Delgado, and A. Morpurgo, *Science* **362**, 324 (2018).

SUPPLEMENTARY MATERIALS OF “MOIRÉ FLAT BANDS OF TWISTED FEW-LAYER GRAPHITE”

I. The term to describe perpendicular electric field in the Hamiltonian of tFL-graphite

In Eq. 1 of the main text, we give the Hamiltonian of the tFL-graphite, where the term U is a diagonal matrix to describe the perpendicular electric field. The effect of a perpendicular electric field is to induce potential difference between layers. We ignore the screening effect and assume that the potential difference distributes uniformly between the top and bottom layers. And, as mentioned in the main text, we set V as the potential difference between two adjacent layers. Let us take the case of 2+4 tFL-graphite for example. Since there are six layers in 2+4 tFL-graphite, the total potential difference between the top and bottom layers is thus $5V$. We then set the potential of top (bottom) layer is $2.5V$ ($-2.5V$). So, $U = \text{diag}(2.5V, 2.5V, 1.5V, 1.5V, 0.5V, 0.5V, -1.5V, -1.5V, -2.5V, -2.5V)$. Note that there are two Bloch basis for each layer, *i.e.*, one is from sublattice A and the other is from sublattice B. So, they have the same potential.

II. Complementary results of tFL-graphite with $N=3$

Moiré bands of AB+ABA and BAB+ABA tFL-graphite—In the main text, we show the moiré bands of the A+ABA, BA+ABA and ABA+ABA in the Fig. 2. Note that there are two remaining configurations of tFL-graphite with $N = 3$, *i.e.*, AB+ABA and BAB+ABA as shown in Fig. S1. Their moiré bands are given in Fig. S2. The only difference between AB+ABA and BA+ABA is the relative orientation of the vdW layers, and their moiré band structures are slightly different. For example, for the AB+ABA [Fig. S2 (b)], two low energy bands (the blue line and the black line) are touching at Γ point, while there is an observable gap in BA+ABA [Fig. 2 (f) of the main text]. The moiré bands of ABA+ABA and BAB+ABA configurations are also slightly different at the γ point.

Unit of the DOS—In order to give an intuitive impression about the order of magnitude of the DOS in the tFL-graphite [see Fig. 2 of the main text], we replot the bands and DOS of A+ABA in Fig. S3, where the unit of DOS is given.

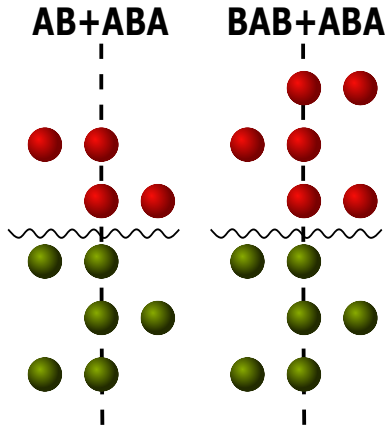


FIG. S1. Side view of tFL-graphite configurations: AB+ABA, BAB+ABA.

Moiré bands calculated with full parameters model—In Fig. 2 of the main text, the moiré bands are calculated with minimal model, where the influence of the remote hopping γ_3 and γ_4 are not considered. Here, we give some results based on full parameters model in Fig. S4, in order to illustrate the more realistic situations. Fig. S4 (a-b) are for A+ABA, (c-d) are for AB+ABA and (e-f) are for ABA+ABA. The first (second) row in Fig. S4 is at $\theta = 1.33^\circ$ (1.05°). First of all, due to the remote hopping, the flat bands become dispersive but their bandwidth are still very small (red solid lines). Meanwhile, the two flat bands are separated in energy, *e.g.*, see Fig. S4 (c,d). Second, a twist angle dependent gap at the Dirac point of the linear bands is induced by γ_3 and γ_4 (blue solid lines). In Fig. S4, the dashed lines are the moiré bands with $\xi = 1$.

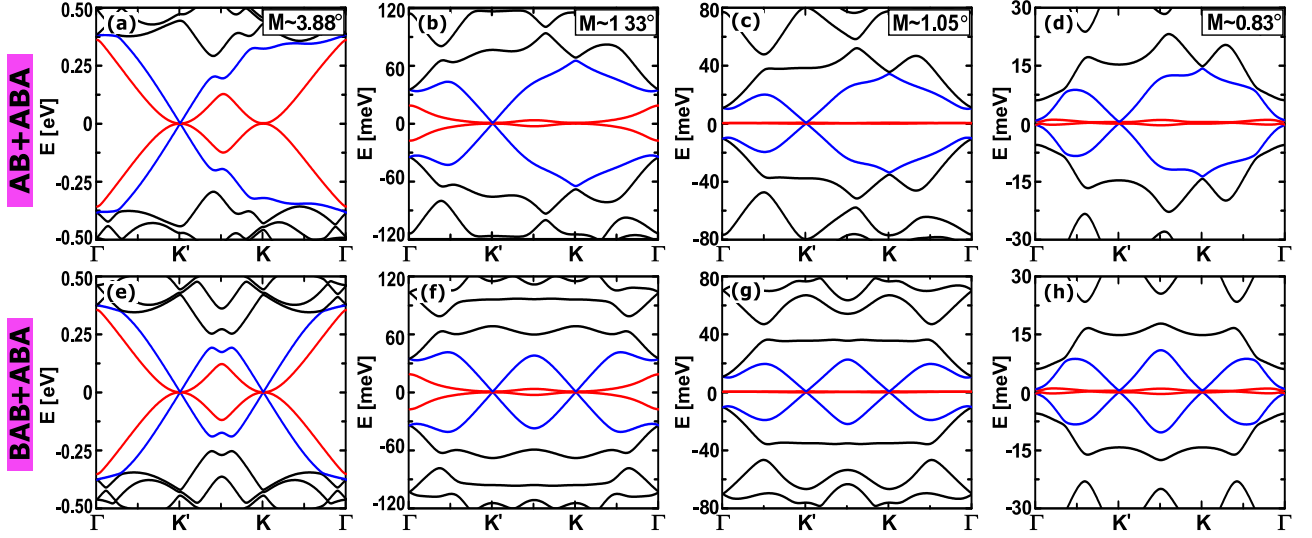


FIG. S2. (a-d) and (e-h) are the moiré bands of the AB+ABA and BAB+ABA, respectively. (a,e) are calculated at $\theta = 3.88^\circ$. (b,f) are calculated at $\theta = 1.33^\circ$. (c,g) are calculated at $\theta = 1.05^\circ$. (d,h) are calculated at $\theta = 0.83^\circ$. Minimal model is used and the parameters are the same as Fig. 2 of the main text.

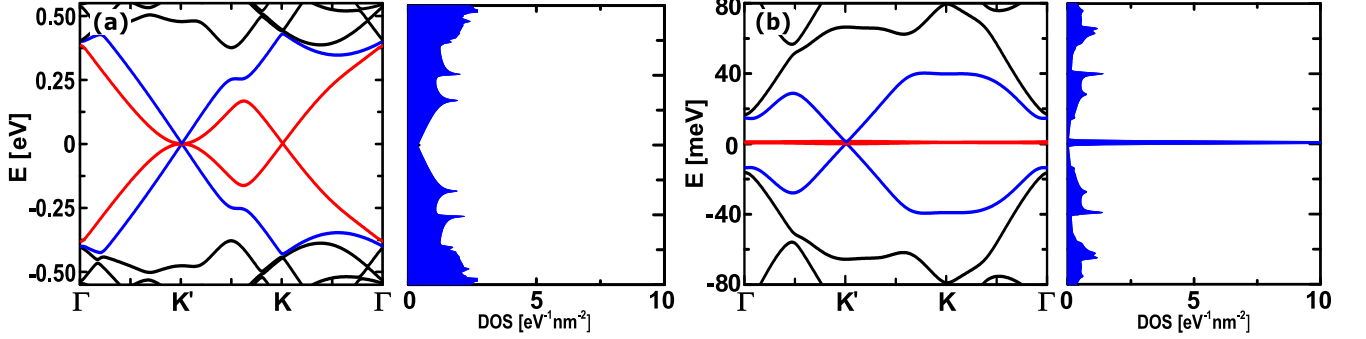


FIG. S3. (a) and (b) are the moiré band (and DOS) of the A+ABA at $\theta = 3.88^\circ$ and $\theta = 1.05^\circ$, respectively. Minimal model is used.

Tunable valley Chern number—In Fig. 3 of the main text, we show that, in ABA+ABA and BAB+ABA, a proper perpendicular electric field can give rise to four isolated nearly flat bands, which have nonzero valley Chern number. The valley Chern number is calculated by the standard formula $C_n = \int_{mBZ} d^2\mathbf{k} \Omega_n(\mathbf{k})/2\pi$, where n is the band index. The Berry connection is

$$\Omega_n(\vec{k}) = -2 \sum_{n \neq n'} \text{Im} \left[\frac{\langle u_n | \frac{\partial H}{\partial k_x} | u_{n'} \rangle \langle u_{n'} | \frac{\partial H}{\partial k_y} | u_n \rangle}{(E_{n'} - E_n)^2} \right], \quad (\text{S1})$$

where $|u_n\rangle$ is the moiré superlattice Bloch state, and E_n is the corresponding eigenvalue.

Such topological flat bands can also be realized in AB+ABA and BA+ABA tFL-graphite, which is shown in Fig. S5. Fig. S5 (a) is the moiré bands of AB+ABA under an electric field $V = 20$ meV at $\theta = 1.33^\circ$, where the valley Chern number of each band is denoted by the black number. That of BA+ABA is given in Fig. S5 (b) with $V = 20$ meV and $\theta = 1.33^\circ$. We see that, though AB+ABA and BA+ABA have similar band structure, but their valley Chern number are different.

The valley Chern number depends on the twist angle and the perpendicular electric field. As an example, we calculate the moiré bands and the valley Chern number of ABA+ABA with various potential difference [$V=10, 20$ meV] and different twist angle [$\theta = 1.33^\circ, 1.05^\circ$], see in Fig. S5 (c-f). Similar phenomenon has been reported in the twisted multilayer graphene with rhombohedral stacking, see Ref. [33-35, 40, 45] of the main text.

Note that in thicker tFL-graphite with $N > 3$, we can not get isolated moiré bands even if a perpendicular electric field is applied, and thus there is no well defined valley Chern number for a single moiré band.

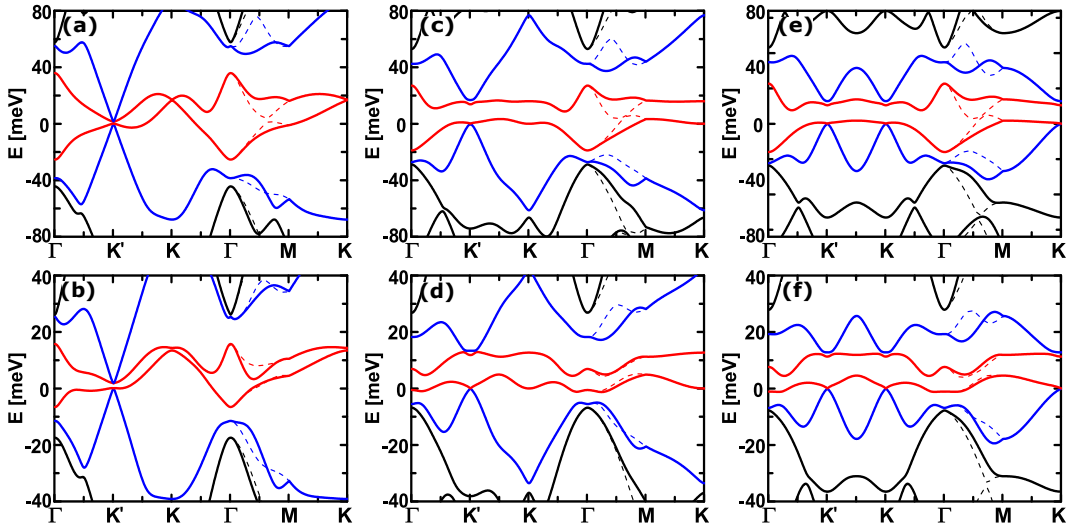


FIG. S4. Moiré bands calculated with full parameter model. (a-b) are for A+ABA, (c-d) are for AB+ABA and (e-f) are for ABA+ABA. (a), (c), (e) are calculated at $\theta = 1.33^\circ$, and (b), (d), (f) are calculated at $\theta = 1.05^\circ$. $\gamma_0/\gamma_1/\gamma_3/\gamma_4 = 2610/360/283/138$ meV.

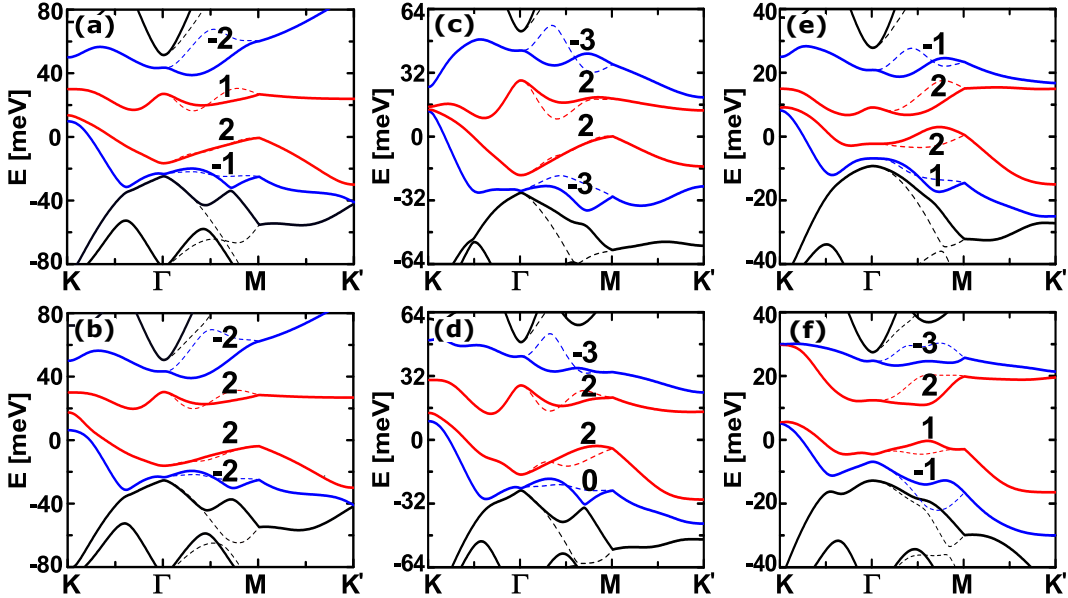


FIG. S5. Moiré bands and valley Chern number in the presence of perpendicular electric field. (a) AB+ABA with $V = 20$ meV and $\theta = 1.33^\circ$. (b) BA+ABA with $V = 20$ meV and $\theta = 1.33^\circ$. (c) ABA+ABA with $V = 10$ meV and $\theta = 1.33^\circ$. (d) ABA+ABA with $V = 20$ meV and $\theta = 1.33^\circ$. (e) ABA+ABA with $V = 10$ meV and $\theta = 1.05^\circ$. (f) ABA+ABA with $V = 20$ meV and $\theta = 1.05^\circ$. The full parameter model is used. Valley Chern numbers are denoted by black numbers and the dashed lines are the moiré bands with $\xi = 1$.

III. Complementary results of the thicker tFL-graphite with $N > 3$

Moiré bands of several related tFL-graphites—In the main text, we have studied the moiré bands of thicker tFL-graphites with $N > 3$. Several typical examples are given in Fig.4, *i.e.*, BA+ABAB, BABA+ABAB, BABA+ABABA. Note that there are several tFL-graphite configurations closely related to these examples, *i.e.*, AB+ABAB, ABAB+ABAB, ABAB+ABABA, where the only difference is the relative orientation of the vdW layers. For comparison, we plot the moiré bands of these related tFL-graphites in Fig. S6.

Electric field influence on the moiré bands—In Fig. 3 of the main text, we show that a perpendicular electric field

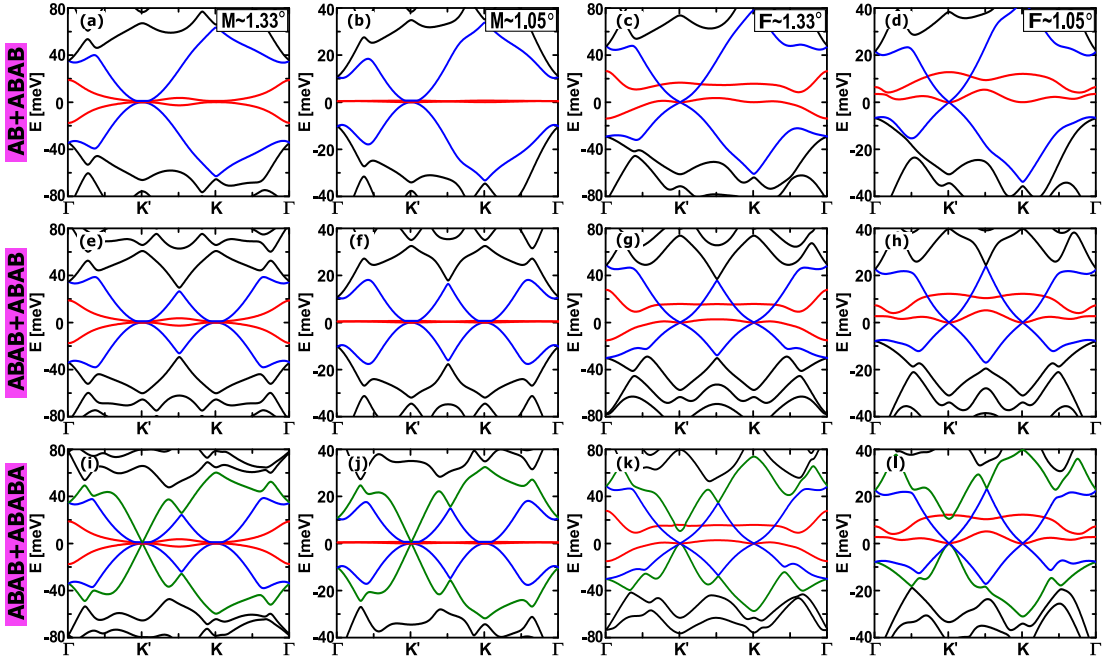


FIG. S6. (a-d), (e-h) and (i-l) are the moiré bands of the AB+ABAB, ABAB+ABAB and ABAB+ABABA, respectively. (a, e, i) are calculated with the minimal model at $\theta = 1.33^\circ$; (b, f, j) are calculated with minimal model at $\theta = 1.05^\circ$; (c, g, k) are calculated with full parameter model at $\theta = 1.33^\circ$; (d, h, l) are calculated with full parameter model at $\theta = 1.05^\circ$. The parameters are the same as the Fig. 4 of the main text.

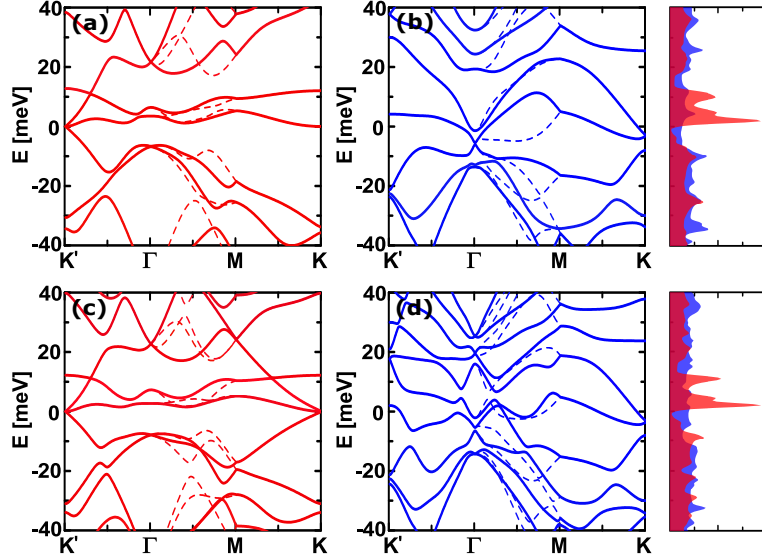


FIG. S7. (a) is the moiré bands of the AB+ABAB with zero electric field at $\theta = 1.05^\circ$ (red), and (b) is that with $V = 20$ meV (blue). (c) is the moiré bands of the ABAB+ABAB with zero electric field at $\theta = 1.05^\circ$ (red), and (d) is that with $V = 20$ meV (blue). The right column is the corresponding DOS, where red is for zero electric field and blue is for finite electric field. Full parameter model is used: $\gamma_0/\gamma_1/\gamma_3/\gamma_4 = 2610/360/283/138$ meV.

can significantly change the moiré bands in the cases of $N = 3$. Actually, a perpendicular electric field also can dramatically modify the moiré bands when $N > 3$. Two examples, *i.e.*, AB+ABAB, ABAB+ABAB, are given in Fig. S7. As a comparison, we first plot the moiré bands of AB+ABAB and ABAB+ABAB with zero electric field at $\theta = 1.05^\circ$ in Fig. S7 (a) and (c), respectively (red lines). Then, an electric field with $V = 20$ meV is applied, and the corresponding moiré bands are given in Fig. S7 (b) and (d), see the blue lines. We see that the band shape, as well as the DOS, is significantly changed by the applied electric field.